RESEARCH ARTICLE

Key Points:
- Direct numerical simulation accurately provides near-interface properties, like interface heat and salt fluxes
- The ratio of heat and salt fluxes varies in free convection strongly with distance from the ice–ocean interface
- The interface flux ratio is 83–100 rather than 33 as determined from previous turbulence measurements

Supporting Information:
- Supporting Information S1
- Figure S1
- Figure S2
- Figure S3
- Figure S4

Correspondence to:
T. Keitzl,
t@keitzl.com

Reconciling estimates of the ratio of heat and salt fluxes at the ice–ocean interface

T. Keitzl[1], J. P. Mellado[1], and D. Notz[1]

[1]Max Planck Institute for Meteorology, Hamburg, Germany

Abstract The heat exchange between floating ice and the underlying ocean is determined by the interplay of diffusive fluxes directly at the ice–ocean interface and turbulent fluxes away from it. In this study, we examine this interplay through direct numerical simulations of free convection. Our results show that an estimation of the interface flux ratio based on direct measurements of the turbulent fluxes can be difficult because the flux ratio varies with depth. As an alternative, we present a consistent evaluation of the flux ratio based on the total heat and salt fluxes across the boundary layer. This approach allows us to reconcile previous estimates of the ice–ocean interface conditions. We find that the ratio of heat and salt fluxes directly at the interface is 83–100 rather than 33 as determined by previous turbulence measurements in the outer layer. This can cause errors in the estimated ice-ablation rate from field measurements of up to 40% if they are based on the three-equation formulation.

1. Introduction

The ice–ocean fluxes are diffusive fluxes. At the ice–ocean interface, no-slip and no-penetration conditions prohibit any turbulent contribution to the exchange of mass, momentum, and energy and what remains is diffusive exchange. Underneath this diffusive interface layer, fluxes are usually dominated by turbulence. The turbulence is sustained because the ocean usually has sufficiently strong a shear underneath the ice. Under freezing conditions, salt release from sea ice amplifies the existing turbulence, while under melting conditions the shear-produced turbulence is somewhat reduced as a result of the meltwater release at the ocean surface stabilizing the water column. Measurements and modeling studies usually focus on this turbulent outer layer and attempt to infer the diffusive fluxes at the interface from the turbulent fluxes. This is because the small spatial extent of the layer dominated by diffusive exchange hinders direct measurements.

In most models, the relationship between the properties of the outer layer and the actual fluxes at the interface are described by the so-called three-equation formulation [*Holland and Jenkins*, 1999]. This formulation improves the ice–ocean heat flux significantly over other simplified formulations [*Schmidt et al.*, 2004]. It requires, however, knowledge of the ratio between the fluxes of heat and salt at the interface. This flux ratio remains uncertain. It has been assessed by various means—by laboratory experiments [*Martin and Kauffman*, 1977], by modeling work [*Holland and Jenkins*, 1999; *Notz et al.*, 2003], and by field observations [*Sirevaag*, 2009]. From these studies, the interface flux ratio, normalized by far-field conditions, can be derived to range between 20 and 90. As demonstrated below, this uncertainty in the flux ratio causes an uncertainty in modeled heat fluxes of up to 40%.

In this contribution, we aim to better understand how the turbulent outer layer interacts with the diffusive interface layer to dictate the heat flux from the ocean to the bottom of sea ice and ice sheets. Although the interaction between the turbulent outer layer and diffusive interface layer is well recognized, its detailed characterization remains a challenge because of the relevance of small-scale features. To address this challenge, we use direct numerical simulation. For numerical convenience, we consider only buoyancy-driven conditions. Although specific scaling laws that we find may change for shear-driven conditions, we believe that the main conclusion remains valid: the flux ratio can vary strongly with distance from the interface and inference of interface properties from outer-layer properties needs to be ascertain with greater detail than has been done so far. We present the details of our simulations (section 4) after we have presented the historic context of the research on the topic (section 2) and defined our idealized system to study it (section 3). By studying separately the molecular and the

turbulent contribution to the vertical structure of the flux ratio (section 5), we explain why all of the formerly assessed flux ratios may be reasonable. Finally, we discuss the interface value of the flux ratio which determines the ice–ocean interface conditions and hence the melt rates (section 6). We find that the interface flux ratio is almost independent of far-field conditions and 3 times as large as the value previously estimated from field measurements. As a result, heat-flux parameterizations based on the three-equation formulation can lead to melt rates overestimated by up to 40%.

2. Formalism

The ratio between heat flux and salt flux is a relevant quantity in the ice–ocean formalism, because it determines the interface values of temperature and salinity, T_i and S_i. This is well illustrated by the boundary conditions of an ice–ocean interface,

$$F_{h,i} = \rho_{ice} w_0 L, \tag{1a}$$

$$F_{s,i} = \rho_{ice} w_0 S_i, \tag{1b}$$

$$T_i = -m S_i. \tag{1c}$$

Because the ice (of density ρ_{ice}) can only dissolve and melt at one particular rate, w_0, the interface salinity must depend on the heat flux, F_h, and the salt flux, F_s, according to equations (1a) and (1b) as $S_i = L F_{s,i}/F_{h,i}$. The index i denotes interface values and L is the latent heat of fusion. From the interface salinity, the interface temperature follows with equation (1c), where m describes the freezing point relation. The challenging part about determining the interface conditions T_i and S_i is a proper representation of the fluxes F_s and F_h at the interface or their ratio.

Josberger [1983] applies both a bulk description and a detailed description based on insights by *McPhee* [1981] to represent these fluxes. From both descriptions, he finds that the interface conditions depend on the far-field conditions and on only one property relating to the flow beneath the ice: the nondimensional ratio of the heat flux to the salt flux at the interface,

$$\gamma_i \equiv \frac{F_{h,i}/\left[c_p(T_\infty - T_i)\right]}{F_{s,i}/(S_\infty - S_i)}, \tag{2}$$

where c_p is the specific heat capacity of water. This ratio describes how effectively turbulence mixes heat compared to salt near the interface. We reproduce the resulting interface salinity from Josberger's three-equation formulation from equations (1a-c) with the commonly used bulk flux parameterizations,

$$F_{h,i} \simeq \rho_{water} c_p \alpha_h u_{*0}(T_\infty - T_i) \text{ and} \tag{3a}$$

$$F_{s,i} \simeq \rho_{water} \alpha_s u_{*0}(S_\infty - S_i), \tag{3b}$$

which are based on the bulk heat exchange coefficient, α_h, the bulk salt exchange coefficient, α_s, and the friction velocity u_{*0} [*Notz et al.*, 2003]. By substituting equations (3a-b) into equations (1a-c), one obtains

$$mS_i^2 + \left(T_\infty + \frac{L}{c_p \gamma_{bulk}}\right) S_i - \frac{L}{c_p \gamma_{bulk}} S_\infty = 0, \tag{4}$$

where $\gamma_{bulk} \equiv \alpha_h/\alpha_s$ is the approximation to γ_i according to equations (3a-b). As discussed by *Josberger* [1983], equation (4) shows that γ_{bulk} is the one flow property that determines the interface conditions from the far-field temperature, T_∞, and far-field salinity, S_∞.

Holland and Jenkins [1999] find from different modeling approaches that $\gamma_{bulk} > 1$ and almost independent of the far-field mean shear velocity. The different model approaches that they employ yield flux ratios γ_{bulk} between 25 and 200 according to their Figure 4.

Notz et al. [2003] take on the determination of γ_{bulk} from field measurements. By modeling observations of false-bottom persistence and migration under sea ice, they indirectly show that γ_{bulk} needs to be substantially different from unity. They adapt results of laboratory studies of fluid heat and mass exchange across hydraulically rough surfaces to describe the dependence of the bulk exchange coefficients on the molecular diffusivities [*McPhee et al.*, 1987]. Within the range they estimate for γ_{bulk} ($35 < \gamma_{bulk} < 70$) [*Yaglom and*

Kader, 1974; *Owen and Thomson*, 1963], they find that a value on the higher end of the range fits their data better.

In sea-ice literature, the bulk exchange coefficients are generally referred to as interface exchange coefficients or turbulent exchange coefficients. The interface fluxes of heat and salt are further approximated by the turbulent fluxes at a certain distance from the interface. In these lines, *Sirevaag* [2009] follows up on the efforts of *Notz et al.* [2003] to determine a turbulent-flux ratio, γ_{turb}, from direct field measurements at a certain distance from the interface. From turbulent-instrument-cluster measurements 1 m beneath the ice–ocean interface in the area of Whaler's Bay, he determines average temperature, salinity, friction velocity, and turbulent fluxes of heat and salt. From his results ($\alpha_h = 1.31 \times 10^{-2}$, $\alpha_s = 4.0 \times 10^{-4}$), he estimates $\gamma_{turb} \approx 33$ (or $\gamma_{turb} \approx 23$ if only data with small mean-temperature changes is accounted for), a value that lies in the opposing end of the range and value given by *Notz et al.* [2003].

As an alternative to bulk parameterizations and turbulent-flux measurements, *Gade* [1993] applies the definitions,

$$F_{h,i} \equiv \rho_{water} c_p \kappa_t \partial_z T|_{z_i}, \text{and} \tag{5a}$$

$$F_{s,i} \equiv \rho_{water} \kappa_s \partial_z S|_{z_i}, \tag{5b}$$

to determine the interface conditions. In line with his procedure, one introduces the gradient thickness of temperature, $\delta_t = (T_\infty - T_i)/\partial_z T|_{z_i}$, and salinity analogously, where the temperature diffusivity, κ_t, and salinity diffusivity, κ_s, are those of water, ∂_z is the vertical derivative, and z_i indicates the position of the ice–ocean interface. One ends up with equation (4), but with γ_{bulk} replaced by the molecular flux ratio at the interface,

$$\gamma_i \equiv Le \ \delta_s/\delta_t, \tag{6}$$

with the Lewis number, $Le = \kappa_t/\kappa_s$. *Gade* [1993] finds a substantially different flux ratio. Based on the experimental work by *Martin and Kauffman* [1977], he determines the boundary thickness ratio,

$$R \equiv \delta_t/\delta_s, \tag{7}$$

to 2.3 which yields an interface flux ratio $\gamma_i = 88.9$, for $\kappa_t = 1.39 \times 10^{-7}$ m²s⁻¹ and $\kappa_s = 6.8 \times 10^{-10}$ m²s⁻¹. This value is significantly different from the turbulent-flux ratio $\gamma_{turb} \sim 33$, which implies a significantly different estimate of the ratio of exchange coefficients.

The uncertainty in the flux ratio leads to considerable uncertainty in the determination of the interface conditions. Whether $\gamma_i \simeq 30$ [*Sirevaag*, 2009] or $\gamma_i \simeq 90$ [*Gade*, 1993] leads to a different determination of the interface salinity according to equation (4) (see Figure 1a). The temperature difference between far field and interface that follows from the different interface salinities is significant. This implies an overestimation of the melt rate by up to 40% with the value of $\gamma_i \simeq 30$ as compared to $\gamma_i \simeq 90$ (see Figure 1b).

3. Setup

In the following, we study a mass of solid ice that floats on top of a body of seawater of fixed uniform temperature $T = T_\infty$ and salinity $S = S_\infty$. Ice and water form an infinite horizontal interface. The ice is isothermal at the freezing temperature of the interface, isohaline at the interface salinity and has a smooth surface. The ice imposes the boundary conditions given in equations (1a-c) on the temperature and salinity fields and no-slip, no-penetration boundary conditions on the flow field. Note that we neglect additional fluxes such as the salt release from sea ice and the heat carried by the melt water, as these will neither in our idealized system nor in the real world significantly influence the general interaction between diffusive and turbulent fluxes that we examine. We consider the ice–ocean interface together with the seawater body as our system of interest.

3.1. The Evolution of the System
This system is purely buoyancy driven and evolves in space and time according to the evolution equations of mass, momentum, internal-energy and solute. With the velocity field $\mathbf{v}(\mathbf{x}, t)$, the temperature field $T(\mathbf{x}, t)$, the salinity field $S(\mathbf{x}, t)$, the spatial coordinate $\mathbf{x} = x_1 \mathbf{e}_1 + x_2 \mathbf{e}_2 + x_3 \mathbf{e}_3$, with $\mathbf{e}_i = \varepsilon_{ijk} \mathbf{e}_j \mathbf{e}_k$, and with time t, these evolution equations are
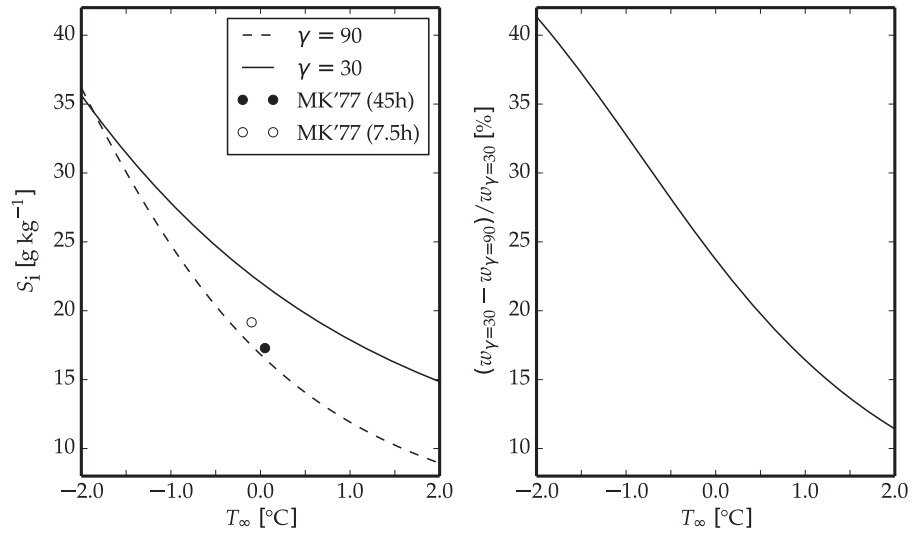
Figure 1. (a) Theoretical interface salinity, S_i, for $S_\infty = 34$ g kg^{-1} and varying T_∞ with $\gamma_i = 30$ or $\gamma_i = 90$. Measured interface salinities 7.5 h (empty dot) and 47 h (filled dot) after laboratory-experiment start [*Martin and Kauffman*, 1977]. (b) Relative difference in melt rate due to difference in interface salinity as seen in Figure 1a. The melt rate, w_0, is given from equation (1a), equation (3a), with $\alpha_h = $ const., $u_{*0} = $ const., and $T_i = T_i(\gamma)$ according to equation (4).

$$\partial_j v_j = 0, \tag{8a}$$

$$\partial_t v_i = -v_j \partial_j v_i + v \partial_j^2 v_i - \partial_i p + b(S, T) \, \delta_{i3}, \tag{8b}$$

$$\partial_t T = -v_j \partial_j T + \kappa_t \partial_j^2 T, \tag{8c}$$

$$\partial_t S = -v_j \partial_j S + \kappa_s \partial_j^2 S. \tag{8d}$$

The equations are given in the Boussinesq approximation. v is the kinematic viscosity, κ_t the thermal diffusivity, κ_s the diffusivity of salinity, p the modified kinematic pressure, ∂_t the temporal derivative, and ∂_i is the spatial derivative in direction of $\mathbf{e}_i$.

The buoyancy, b, depends on both temperature and salinity. We follow previous numerical work on double-diffusive systems [*Nagashima et al.*, 1997; *Gargett et al.*, 2003; *Kimura and Smyth*, 2007; *Zweigle*, 2011; *Carpenter et al.*, 2012] and approximate the buoyancy to first order by

$$b(S, T) \equiv \frac{g}{\rho_{\text{water}}} [\beta(S_\infty - S) - \alpha(T_\infty - T)], \tag{9}$$

where g is earth's gravitational acceleration, α is the thermal expansion coefficient, β is the haline contraction coefficient, and ρ_{water} is the water density. The subscript $_\infty$ denotes the values in the far field, i.e., far enough from the interface for the seawater properties to be approximately homogeneous. The salinity component of the buoyancy stabilizes the water column for values $S < S_\infty$, the temperature component destabilizes the water column for values $T < T_\infty$. From the interplay of both salinity and temperature at different diffusivities follows a buoyancy-reversal instability that forces the system. The flow develops freely into the far field (see Figure 2). It does not feel any solid boundary but the ice–water interface.

For sufficiently low viscosity, the system becomes turbulent, decorrelates from its initial state after a sufficiently long time, and solely depends on the set of control parameters $\{v, \kappa_t, \kappa_s, g\, \rho_{\text{water}}^{-1} \alpha\, (T_\infty - T_i), g\, \rho_{\text{water}}^{-1} \beta\, (S_\infty - S_i)\}$. Dimensional analysis provides the set of nondimensional, independent control parameters $\{\text{Pr}, \text{Le}, R_\rho^s\}$, with Prandtl number $\text{Pr} = v/\kappa_t$, Lewis number $\text{Le} = \kappa_t/\kappa_s$, and density ratio

$$R_\rho^s \equiv \frac{\beta(S_\infty - S_i)}{\alpha(T_\infty - T_i)} \tag{10}$$

[*Turner*, 1974]. For any given fluid of fixed Pr and fixed Le, any flow property does only depend on the governing parameter R_ρ^s, once the initial conditions have been sufficiently forgotten. R_ρ^s quantifies the
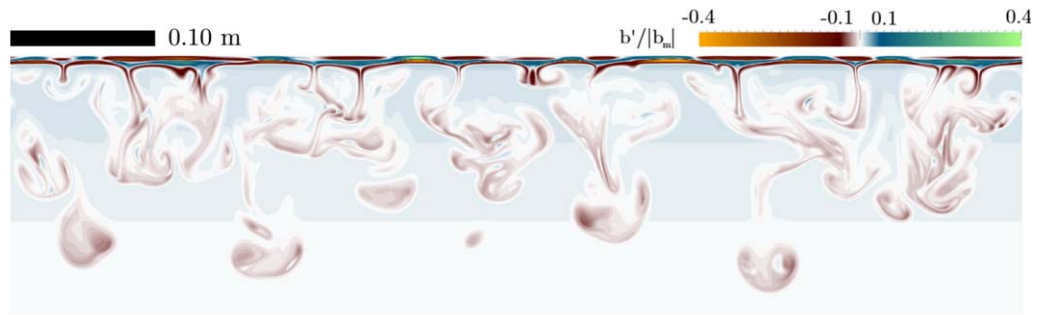
Figure 2. Simulated buoyancy fluctuations at final simulation time for Pr=10, Le=4, and R_ρ^s=6 (see Table 1). The blue shaded regions represent the stable background stratification due to the chosen initial salinity profile.

stabilizing effect of the salinity component of the buoyancy compared to the destabilizing effect of the temperature component. Equation (9) is then written as

$$\frac{b}{|b_m|} = R_\rho^s\ \sigma - \theta, \tag{11}$$

with the minimum buoyancy $b_m \equiv b(S_\infty, T_i) = g\rho_{water}^{-1}\alpha(T_\infty - T_i)$, the normalized temperature θ, and the normalized salinity σ,

$$\theta \equiv \frac{T_\infty - T}{T_\infty - T_i}, \tag{12a}$$

$$\sigma \equiv \frac{S_\infty - S}{S_\infty - S_i}. \tag{12b}$$

We assess the range of validity of equation (11) from a parametric plot $b = b(S, T)$ that we compare to the proper formulation by *Sharqawy et al.* [2010] (not shown). For $R_\rho^s > 5$, equation (11) becomes increasingly good an approximation with absolute buoyancy deviations less then 0.20 $|b_m|$.

The fully developed turbulent system is statistically homogeneous in horizontal directions. We denote horizontally averaged quantities by $\langle \cdot \rangle$ and fluctuations around that mean by $\cdot'$. Horizontally averaged statistics only depend on $\{R_\rho^s;\ z, t\}$ with $z = - \ \boldsymbol{x} \cdot \boldsymbol{e}_3$ and the origin of $\boldsymbol{x}$ chosen such that z gives the distance from the interface.

3.2. The Boundary Conditions

The boundary conditions, equations (1a-c), are Robin boundary conditions. The interface temperature and the interface salinity, $T_i = -mS_i$ and $S_i = L\ F_{s,i}/F_{h,i}$, depend on fluxes, F_s and F_h, at the interface. The fluxes evolve with the flow and so do the boundary conditions. We simplify the boundary conditions encountered in nature in two respects.

First, we apply homogeneous and steady Dirichlet boundary conditions at the top boundary of the scalar fields. Therefore, the system does only reflect a natural evolution of the flow once the interface flux ratio has reached an equilibrium, when the interface temperature and interface salinity are steady and do no longer vary as the flow evolves in time. The tendency of a similar system to relax toward a preferred interface flux ratio has been observed before by *Carpenter et al.* [2012]. In the supporting information, we show that the flux ratio does also relax toward an equilibrium in our simulations.

Second, we do not incorporate meltwater formation. According to *Keitzl et al.* [2016], meltwater formation only influences the flow structure when the Richardson number,

$$\mathrm{Ri}_0 = b(z_i)/|b_m| + 1, \tag{13}$$

approaches one. This Richardson number describes the importance of the stable stratification next to the interface, where $b(z_i) = b(S_i, T_i)$ is the interface buoyancy, compared to the strength of the buoyancy reversal that drives the convection, $|b_m|$. This Richardson number relates to the density ratio R_ρ^s of the setup described in the present paper because, according to equation (11), we have

$$Ri_0 = R_\rho^s. \tag{14}$$

One can hence expect that R_ρ^s similarly describes the importance of the stable stratification next to the interface compared to the strength of the buoyancy reversal. For their free-convection system, *Keitzl et al.* [2016] find that meltwater formation can be neglected as long as convective motions driven by the buoyancy reversal cannot overcome the stable stratification next to the ice, that is as long as $R_\rho^s \gg 1$.

The reason for this small effect of the melt water is the following. For a quasi-steady regime near the surface, the melt of water can be considered analytically by changing the kinematic boundary condition from no-penetration to a nonzero normal velocity at the interface, by defining the problem in a frame of reference moving with the interface at a velocity equal to w_0. Such a kinematic condition implies an advective flux of heat in addition to the molecular flux. As explained in *Keitzl et al.* [2016], this advective flux is small compared with the molecular flux as long as the Richardson number is small, and can be neglected. We restrict our investigations to such systems.

4. Direct Numerical Simulation

We integrate equations (8) using a high-order finite difference method on a collocated, structured grid. We approximate the integration by a fourth-order Runge-Kutta scheme and the spatial derivatives by sixth-order spectral-like finite differences [*Williamson*, 1980; *Lele*, 1992]. After every integration step, a pressure solver ensures fulfillment of the solenoidal constraint. For this, we use a Fourier decomposition along periodic horizontal coordinates and a factorization of the resulting second-order equations in the vertical coordinate [*Mellado and Ansorge*, 2012].

The calculations are performed on a grid of 1152 grid points in the vertical direction and 2560 grid points in both horizontal directions. The grid spacing is uniform in the horizontal directions $\mathbf{e}_1$, $\mathbf{e}_2$ and in most of the vertical direction $\mathbf{e}_3$. The resolution in $\mathbf{e}_3$ close to the interface, however, is increased because the main mean-temperature and mean-salinity variation all over the domain occurs close to the interface. These variations potentially entail the main mean-buoyancy change, a change in the forcing of the system from a positive to the global-extreme negative value and back to almost zero. To fully cover this buoyancy variation, we increase the resolution next to the interface by a factor of two and a half [*Mellado*, 2012]. The regions of uniform and adjusted resolution in $\mathbf{e}_3$ are gradually matched by hyperbolic tangents. Finally, the grid in $\mathbf{e}_3$ far from the interface is coarsened to save computing time. This part of the domain serves to diminish the influence of the computational boundary on the flow. This grid spacing, Δx_3, holds $\Delta x_3/\eta_B < 2.0$ at all times where η_B is the Batchelor scale.

The boundary conditions in the velocity field are no-slip and no-penetration at the interface, and free-slip and no-penetration in the far field. The boundary conditions in the temperature and salinity field are Dirichlet at the interface and Neumann in the far field. The initial conditions are an error-function profile in the temperature and salinity fields and zero in the velocity field. The error-function profiles are described by their gradient thicknesses, δ_s and δ_t, at initial time. The profiles of temperature, salinity, and flow fields are perturbed by broadband fluctuations to accelerate the transition to turbulence. The initial boundary thickness ratio, $R_{init} = R(t=0)$, remains the most influential parameter of the initial conditions. A value around 1.5 or below forces a diffusive evolution in the beginning. A larger value forces the system with a buoyancy-reversal instability due to the opposing forcing mechanisms of temperature and salinity.

We are particularly interested in simulations of Pr between 10 and 13.8 and Le between 176 and 204 that resemble cold ocean-like fluids [*Steele et al.*, 1989; *Notz et al.*, 2003; *Schmidt et al.*, 2004; *Sharqawy et al.*, 2010]. The available computational resources, however, constrain our investigations to Pr×Le=40 for which turbulence is still fully resolved on diffusive scales. In total, we run 6 three-dimensional simulations (three on the influence of initial conditions by varying R [see supporting information] and three on the influence of R_ρ^s). For our main simulations, we stick to a water-like fluid of Pr=10 but of limited Le=4. The main simulation runs explore the influence of varying $R_\rho^s \in \{6, 11, 21\}$ (see Table 1). The estimated final boundary layer height of the simulated systems, z_{est}, is about 0.2 m (see Table 1). The simulations reach Reynolds numbers $w_* z_{est} v^{-1}$ and $e^2(\varepsilon v)^{-1}$ of up to 350 and 25, respectively, with the turbulent kinetic energy e, the viscous dissipation rate ε, the convective velocity scale, w_* and the viscosity v. The convective velocity scale, w_*, is a measure for the velocity scale within the convective region. It is defined as

Table 1. Properties of the Numerical Simulations of the Ice–Ocean System[a]

R_ρ^s	Pr	Le	T_∞ (°C)	$\lvert b_m \rvert$ (m s^{-2})	z_{est} (m)	$\frac{w_* z_{est}}{\nu}$	$\frac{e^2}{(\varepsilon \nu)}$	R_{final}
6	10	4	24.0	4.51×10^{-2}	0.17	348	25	1.67
11	10	4	16.1	2.45×10^{-2}	0.17	245	18	1.80
21	10	4	10.4	1.27×10^{-2}	0.19	192	13	1.89

[a]The set of the first three columns uniquely defines the system. They are the density ratio, R_ρ^s, the Prandtl number Pr, and the Lewis number Le. All figures of this study will use the colors black ($R_\rho^s = 6$), light blue ($R_\rho^s = 11$), and dark blue ($R_\rho^s = 21$) to refer to the simulations. The following two columns provide the far-field temperature and the minimum buoyancy for the reader's convenience. The far-field temperature, T_∞, is determined from equation (4) with $S_\infty = 34$ g kg^{-1} and $R = 2.3$ at Le $= 200$. The minimum buoyancy is $b_m = b(S_\infty, T_i)$. The columns 6–9 characterize the turbulent system in its stage of final simulation time. The simulations reach a boundary layer height, z_{est}, of up to 0.19 m, and the convective Reynolds numbers, $\frac{w_* z_{est}}{\nu}$, of up to 350, and turbulent Reynolds numbers, $Re_{turb} = e^2 / (\varepsilon \nu)$ of up to 25, with turbulent kinetic energy e, viscous dissipation rate ε and viscosity ν. The convective velocity scale, w_*, is defined as $w_*^3 = \int_0^\infty \mathcal{H}(\langle b' v_3' \rangle) \langle b' v_3' \rangle dz$, where $\mathcal{H}$ is the Heavyside function. The last column is the resulting boundary thickness ratio of the simulation, R. All simulations have been initialized with an initial boundary thickness ratio of $R = 2$. The grid size of the simulations is $2560 \times 2560 \times 1152$. At final time of the simulations, the boundary layer reaches an aspect ratio between 4:1 and 5:1.

$w_*^3 = \int_0^\infty \mathcal{H}(\langle b' v_3' \rangle) \langle b' v_3' \rangle dz$, where $\mathcal{H}$ is the Heavyside function. This expression for the convective velocity scale w_* is obtained from the inviscid scaling of the viscous dissipation rate $\varepsilon \propto w_*^3\, z_{est}^{-1}$ [*Pope*, 2000] and the observation that

$$\frac{\int_0^\infty \varepsilon\, dz}{\int_0^\infty \langle b' v_3' \rangle\, dz} \approx 0.77 \qquad (15)$$

in our simulations.

To circumvent the computational constraints of three-dimensional simulations, we further conduct 21 two-dimensional simulations. The two-dimensional simulations contribute additional evidence in the region of the parameter space accessible to the three-dimensional simulations, and allow us to extrapolate into other regions of the parameter space: Six simulations of Pr $= 1$ approach the behavior of varying Le up to Le $= 160$. Five simulations each of Pr $= 6$ and Pr $= 10$ approach the behavior of varying Le up to Le ≈ 20. An additional five simulations confirm similar results for the interface fluxes between three-dimensional and two-dimensional simulations (see supporting information).

5. The Nondimensional Flux Ratio

From the full expressions of the heat flux and the salt flux,

$$F_h(z, t) \equiv -\rho_{water} c_p \left(\kappa_t \partial_3 \langle T \rangle (z, t) - \langle v_3' T' \rangle (z, t) \right) \text{ and} \qquad (16a)$$

$$F_s(z, t) \equiv -\rho_{water} \left(\kappa_s \partial_3 \langle S \rangle (z, t) - \langle v_3' S' \rangle (z, t) \right), \qquad (16b)$$

one obtains the nondimensional flux ratio,

$$\gamma(z, t) \equiv \frac{\kappa_t \partial_3 \langle \theta \rangle (z, t) - \langle v_3' \theta' \rangle (z, t)}{\kappa_s \partial_3 \langle \sigma \rangle (z, t) - \langle v_3' \sigma' \rangle (z, t)}, \qquad (17)$$

with the normalized temperature, θ, and the normalized salinity, σ. Particularized at the interface, we recover γ_i, defined in equation (2).

We can further define a turbulent-flux ratio and a molecular flux ratio. The turbulent-flux ratio is

$$\gamma_{turb} \equiv \frac{\langle v_3' \theta' \rangle (z, t)}{\langle v_3' \sigma' \rangle (z, t)}, \qquad (18)$$

and is identical to the ratio of turbulent exchange coefficients of *Notz et al.* [2003] and *McPhee et al.* [2008] if the interface flux ratio is approximated by the mean turbulent-flux ratio. Note that the heat and salt fluxes in equation (18) are normalized by the energy and salt variation across the boundary layer; hence, for a given boundary layer depth, the ratio in equation (18) is a good approximation to the ratio of the fluxes normalized by the mean gradients, i.e., the ratio of heat to salt turbulent diffusivities. The molecular flux ratio is
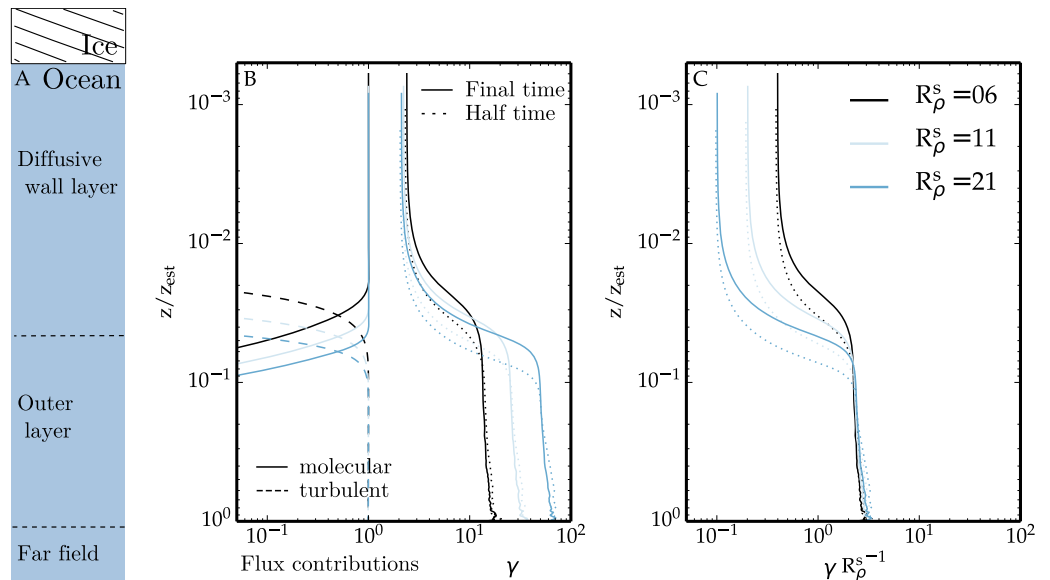
Figure 3. (a) Illustration of the vertical structure of free convection beneath a melting ice–ocean interface. (b) Molecular fraction of total heat transport (solid line on the scale < 1.0) and turbulent fraction of total heat transport (dashed line on the scale < 1.0). Ratio between the total heat transport (molecular + turbulent) and the total transport of salinity, γ, at final simulation time (solid line on the scale > 1.0) and at half simulation time (dotted line on the scale > 1.0). This figure shows that γ_{turb} describes this spatial structure well in the outer layer, γ_{mol} describes it well next to the interface. (c) Ratio γ at final simulation time, but scaled with R_ρ^s. Colors indicate different density ratios, R_ρ^s: black (R_ρ^s=6), light blue (R_ρ^s=11), and dark blue (R_ρ^s=21).

$$\gamma_{\mathrm{mol}} \equiv \mathrm{Le}\,\frac{\partial_3 \langle \theta \rangle (z,t)}{\partial_3 \langle \sigma \rangle (z,t)} \qquad (19)$$

and has been used by *Gade* [1993] to determine the interface conditions. The approximation to reduce the flux ratio either to γ_{mol} at the interface or γ_{turb} in the outer layer is reasonable, because there the corresponding contributions to the fluxes dominate numerator and denominator of γ (see Figure 3b).

The determination of the interface conditions, however, requires that γ is evaluated at the interface, i.e., $\gamma_i \equiv \gamma|_{z_i}$. Hence, the interface conditions depend solely on the molecular flux ratio, because the turbulent flux at the interface is zero. The use of γ_{turb} in the turbulent outer layer as a surrogate for γ_{mol} in the diffusive interface layer is convenient, because it allows for the employment of turbulent-flux measurements from the field. With our simulations we find, however, that in the semiconvective regime γ_{turb} is not a good proxy for γ_{mol} at the interface. Even though $\gamma_{\mathrm{turb}} \neq \gamma_{\mathrm{mol}}$, it might still be valid to employ turbulent-flux measurements once the relation between turbulent and molecular flux ratio is clarified. In the following, we explore the vertical structure of γ from our simulations to understand this relation.

5.1. Vertical Structure of the Flux Ratio

The vertical structure of free convection beneath a melting, horizontal, smooth ice–ocean interface in the semiconvective regime is well described by a two-layered structure: a diffusion-dominated interface layer (the diffusive interface layer) and a turbulence-dominated outer layer (in sea-ice literature sometimes referred to as mixed layer) (see Figure 3a). Molecular diffusion dominates the heat transport next to the interface (see Figure 3, solid line on the scale < 1.0). Turbulent transport dominates the heat transport in the outer layer (see Figure 3, dashed line on the scale < 1.0). This description is similar to the two-layered structure of the freshwater system, a free-convection system beneath a melting, horizontal, smooth ice–water interface [*Keitzl et al.*, 2016]. This two-layer structure is inspired by the more detailed description of the boundary layer of free convection over a heated plate in *Mellado* [2012]. In this section, we use results from the three-dimensional simulations with Le=4 to find the scaling laws of the nondimensional flux ratio in each of these two layers as a function of the nondimensional control parameters introduced in section 3.1.

Within the diffusive interface layer, we observe that the nondimensional flux ratio remains approximately constant with respect to z and thus equal to the interface value, γ_i (see Figure 3b, solid lines on the scale > 1.0). Besides, the flux ratio remains approximately steady and only weakly dependent on the far-field conditions (represented by varying R_ρ^s). Quantitatively, it proves convenient to express the interface flux ratio in terms of the boundary thickness ratio, $R(\mathrm{Pr}, \mathrm{Le}, R_\rho^s)$, because R removes the leading order dependence of γ_i on Le [see equations (6), and (7)]:

$$\gamma_i = \mathrm{Le}\ R(\mathrm{Pr}, \mathrm{Le}, R_\rho^s)^{-1}. \tag{20}$$

(We will show below that indeed the dependence of R on Le is relatively weak, with changes in R of order one when Le changes over two orders of magnitude.) We measure $R \sim 1.7-1.9$, which for the case Le=4 considered in this section implies $\gamma_i \sim 2$, as observed in Figure 3. This constant value of R can be interpreted as a layer of strong mean-salinity variation embedded into a slightly thicker layer of strong mean-temperature variation. The visualizations indicate, however, that temperature-driven and salinity-driven buoyancy fluctuations alternate next to the interface (see Figure 2).

In the outer layer, the nondimensional flux ratio is different from γ_i: for the case Le=4 considered in this section, it is larger (see Figure 3b, solid lines on the scale > 1.0). The scaling laws with respect to the control parameters are also different: the flux ratio depends on the far-field conditions (cf. varying flux ratio for varying R_ρ^s). This dependence can be explained as follows. From the definition of the turbulent-flux ratio, γ_{turb} [see equation (18)], one expects it to be independent of the diffusivity ratio, Le, and to scale with a certain temperature-salinity ratio θ/σ. If the outer layer is well mixed, temperature and salinity will be distributed homogeneously. Their mixing is driven by a buoyancy-reversal instability. According to equation (11), the buoyancy-reversal instability is favored by a temperature-salinity ratio commensurate with the density ratio, R_ρ^s, i.e., $\theta/\sigma \sim R_\rho^s$ (see supporting information). Consequently, temperature and salinity must be entrained in a proportion that is commensurate with this R_ρ^s to maintain this θ/σ. Our simulations support this argument and provide the scaling

$$\gamma_{\mathrm{turb}} = 2.3\ R_\rho^s \tag{21}$$

(see Figure 3c).

5.2. Temporal Evolution of the Fluxes and Their Ratio

The vertical structure of the flux ratio results from the vertical structure of the temperature and salinity flux. All of our simulations exhibit a similar vertical flux structure: the molecular fluxes at the interface are higher than the turbulent fluxes in the outer layer (cf. Figure 3, supporting information). As a consequence of this vertical flux structure, the flux profiles are not steady. The water near the interface continuously cools and freshens, the diffusive interface layer thickens, and the molecular fluxes of temperature and salinity at the interface decrease.

While the molecular fluxes at the interface keep decreasing in time, we observe a quasi-steady flux ratio that is described by R near the interface and by R_ρ^s in the turbulent outer layer. Accordingly, we observe that the turbulent fluxes decrease along with the molecular fluxes for all of our simulations. The vertical integral of the molecular and turbulent fluxes, and hence the convective velocity scale, stagnates as the boundary layer grows (not shown). This behavior implies that mixing across the turbulent boundary layer becomes slower (the time scale z_{est}/w_* increases), and the system becomes more sensitive to external perturbation, e.g., instabilities driven by mean shear or horizontal advection of water masses with different far-field properties.

For shear-driven flows, the behavior of the flux ratio remains an open question. However, several arguments indicate that the properties observed in this study might be independent of the details of the forcing. First, free-convection setups intrinsically feature shear due to convective motions of various length scales that form next to the interface [e.g., see *Mellado et al.*, 2016]. Second, next to the interface, much of the interaction between temperature and salinity is determined by the interplay of diffusive processes, independent of the forcing. Third, while we change the initial turbulent kinetic energy of our system with varying initial conditions, the system always tends toward one particular flux ratio (cf. Figure 1 in the supporting information).

In summary, the quasi-steady vertical structure of the flux ratio is well described by two parameters. A boundary thickness ratio, R, describes the molecular flux ratio at the interface. A density ratio, R_ρ^s, describes the turbulent-flux ratio in the outer layer. Because R_ρ^s is an independent control parameter that defines the setup, only R remains to be determined to know the vertical structure of the flux ratio.

6. Discussion

In this work, we have expressed the interface flux ratio γ_i in terms of the boundary thickness ratio R [equation (6)], and we have so far determined R from simulations at fixed Pr=10 and fixed Le=4. We have learned that R can be described by a quasi-steady value, independent of the initial conditions (see supporting information) and only weakly dependent on the far-field conditions. We will now use former studies along with a series of two-dimensional simulations for varying Prandtl number and Lewis number to assess the boundary thickness ratio at as high a Lewis number as it occurs in the Arctic Ocean.

Two-dimensional turbulence and three-dimensional turbulence differ in many aspects. However, simulations of two-dimensional turbulent convection appear to yield an energy balance at the interface that is within 10% of that of three-dimensional simulations. This has already been observed for simulations of the freshwater system (not shown), and it is so for the simulations of the ice–ocean system in both temperature and salinity. *Carpenter et al.* [2012] have shown that two-dimensional direct numerical simulation accurately captures the heat flux and interface structures of three-dimensional direct numerical simulations when the density variation due to salinity is at least 3 times larger than the density variation due to temperature. Besides, two-dimensional simulations have been employed before to study three-dimensional systems. *Johnston and Doering* [2009] for example report very similar heat-flux scaling laws between two-dimensional and three-dimensional Rayleigh-Bénard convection. They further comment on a finding of a recent high-resolution study that "statistical and bulk transport properties of the flows may correspond quantitatively, at least at sufficiently high Prandtl number."

From the collection of two-dimensional and three-dimensional simulations (see Figure 4), it emerges that R increases with increasing Lewis number, Le. In other words, the larger the difference of temperature diffusivity and salinity diffusivity is, the larger the difference in their gradient thicknesses. The diffusivity, κ, of the scalar that defines the buoyancy is a key parameter in the diffusive interface layer in free-convective flows next to a Dirichlet interface. The corresponding gradient thickness, δ, scales as $\kappa^{2/3}$ [*Mellado*, 2012]. One might therefore expect the ratio of two gradient thicknesses which are controlled by different diffusivities to scale with the ratio of diffusivities as $(\kappa_t/\kappa_s)^{2/3}$ as long as the two scalars do not couple to each other (see Figure 4, dashed line).
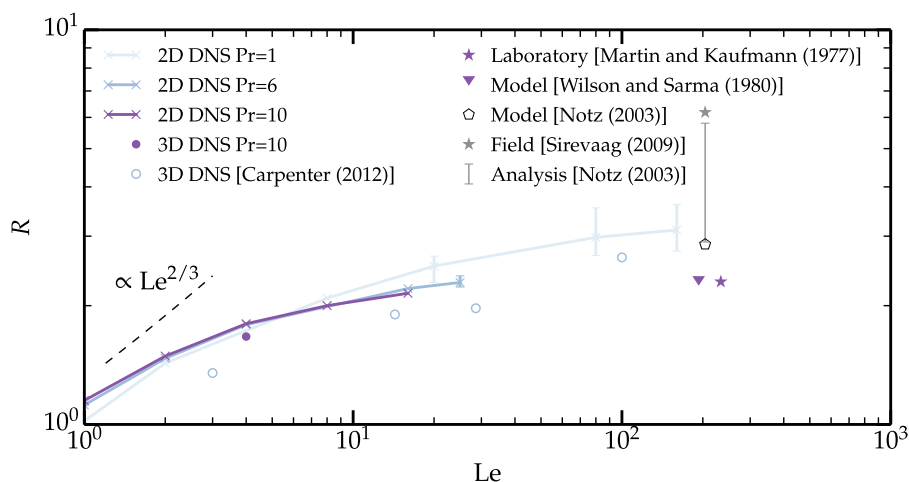

Figure 4. Lewis-number series of boundary thickness ratio, $R=\delta_t/\delta_s$. Colors indicate different Prandtl numbers: Pr=1 (light blue), Pr=6.25 (blue), Pr=10 (purple). For clarity, the figure only contains simulations with $R_\rho^s=6$ and $R_{init}=2$. The error bars in the simulation data indicate the maxima and minima of the temporal fluctuations around the mean value. The dashed line indicates the expected behavior of R from the diffusive scalings of free convection over a heated plate. The data of Pr=10 (purple) suggest a boundary thickness ratio of 2–2.3.

Interestingly, R levels off with further increasing Le indicating that the temperature and salinity field interact with each other (see Figure 4). *Carpenter et al.* [2012] reason that the temperature profile effectively feels the salinity interface as a solid conducting plane once Le is high enough. Then, the development of a temperature sublayer at this apparent salinity interface should only depend on the Prandtl number. For a fixed Prandtl number, it is hence reasonable to expect that the boundary thickness ratio approaches a constant. We observe that R still depends on the diffusivity of the more strongly diffusing scalar, temperature. Our simulations are consistent with the scaling, $R \propto \mathrm{Pr}^{2/3}$, suggested by *McPhee et al.* [1987] (see Figure 5). For Pr=10, a Le of four already seems to be high enough to approach independence of R on Le. From our simulation, we measure $R = 1.7$–1.9. That yields $\gamma_{\mathrm{mol}} = 105$–$118$ for typical Arctic conditions with Le $\simeq 200$.

6.1. Comparison to Former Studies

The range of values of the boundary thickness ratio obtained in our simulations, $R = 1.7$–1.9, is consistent with estimates from previous studies.

Notz et al. [2003] assessed the bulk flux ratio by modeling observations. They use this bulk flux ratio to determine the interface temperature and salinity. In this sense they equate γ_{bulk} with γ_{i}. This hypothetical equality implies a hypothetical boundary thickness ratio, R. The range they estimate for γ_{bulk} corresponds to a R range of $[2.9 < R < 5.7]$ (see Figure 4, grey bar). However, their hint that lower R values fit the data better already points toward the smaller value obtained in this study.

Carpenter et al. [2012] assessed the flux ratio of a fluid-fluid interface—warm and fresh fluid on top of cold and salty fluid by numerical experiments. Buoyancy-reversal instabilities on both sides of a sharp fluid-fluid interface promote free convection. They find that turbulence is not able to penetrate the stable stratification of the interface core. Just like a solid interface, their fluid-fluid interface is dominated by molecular fluxes. They observe a boundary thickness ratio, R, of 2.5 at Pr=6.25, Le=100, $R_\rho^s = 6$ (see Figure 4, circle), similar to the values observed in our simulations. They also measured the flux ratio across a fluid-fluid interface during a field campaign at Lake Kivu [*Sommer et al.*, 2013]. From nearly ten thousand microstructure measurements across staircases they obtain a distribution of observed flux ratios. This distribution also peaks around $R = 2$ (see Figure 6f therein).

Gade [1993] assessed the molecular flux ratio from the boundary thickness ratio of interfacial profiles of temperature and salinity. He finds $R = 2.3$ from the laboratory work of *Martin and Kauffman* [1977] (see Figure 4, purple star) and $R = 2.26$ from the modeling work of *Wilson et al.* [1980] (see Figure 4, pyramid).

Hence, we estimate a boundary thickness ratio of

$$R = 2.2 \pm 0.2 \tag{22}$$

from all of the evidence presented so far: from the trends of all two-dimensional simulations to lose their dependence on the Lewis number (see Figure 4, l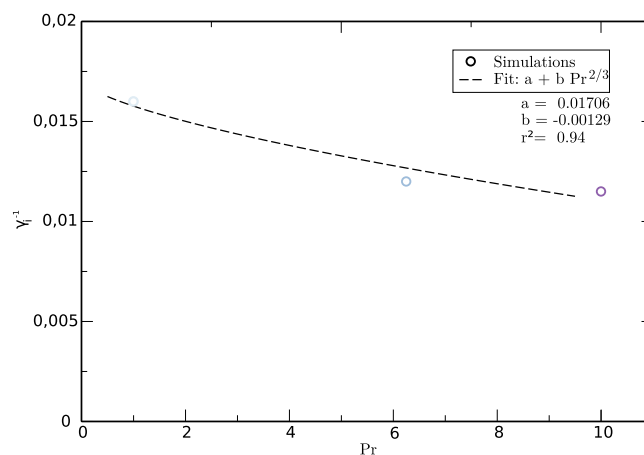ines), from the value which the two-dimensional simulations approach for increasing Lewis number at Pr=10 (purple line), from the laboratory-experiment value of *Martin and Kauffman* [1977] (purple star), and from the fact that the three-dimensional simulation yields a slightly smaller value than does the two-dimensional simulation (purple dot). This interval yields an interface flux ratio in the range of 83–100 for typical Arctic conditions with Le $\simeq 200$. The interface flux ratio determined in this work does agree with that obtained from laboratory work, modeling work and numerical work of similar setups.

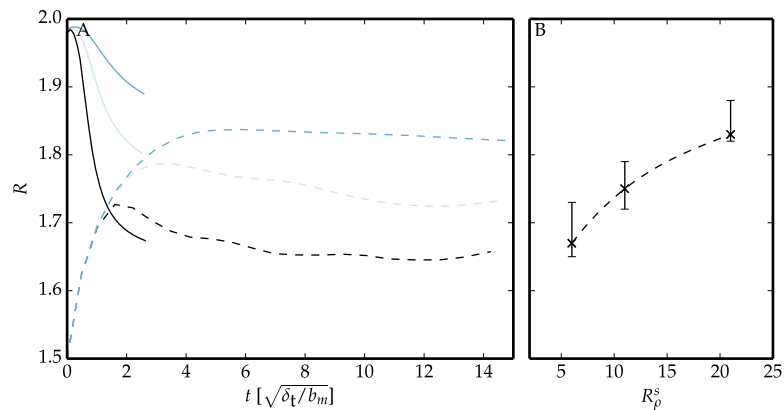The interface flux ratio has been suspected to depend on the surface

Figure 5. Simulated γ as extrapolated from Figure 4 for Le ≈ 200 (circles) and power law prediction by *McPhee et al.* [1987] (dashed line). Colors indicate different Prandtl numbers: Pr=1 (light blue), Pr=6.25 (blue), and Pr=10 (purple).

Figure 6. (a) Evolution of the boundary thickness ratio in time. Three-dimensional simulations (solid lines) approach the values obtained from two-dimensional simulations (dashed lines). Colors indicate the density ratio of the simulation as given in Figure 3c. (b) Density-ratio series of the boundary thickness ratio.

roughness of the ice–ocean interface [*Notz et al.*, 2003]. Our investigations of a smooth ice–ocean interface show that in principle no surface roughness at all is needed to reproduce the turbulent-flux ratios that have been suggested as reasonable.

6.2. Dependence of the Boundary Thickness Ratio on Far-Field Temperature and Salinity

So far it seems that the boundary thickness ratio is a universal property of a melting ice–ocean interface. However, a weak dependence on the far-field conditions remains. As explained in section 2, the far-field conditions reflect in the overall temperature range, $T_i - T_\infty$, and in the overall salinity range, $S_i - S_\infty$, of the system. Hence, the independent control parameter that characterizes the far-field conditions is the density ratio, R_ρ^s. The dependence of R on R_ρ^s is illustrated in Figure 6. The variation in R accounts for about 10% of its value.

We have only provided the dependence of the boundary thickness ratio on the density ratio for a very narrow range. We are confident, however, that the results of the restricted parameter space hold for higher density ratios for two reasons. First, the dependence is faint and seems to level off for increasing R_ρ^s. Second, the laboratory experiment of *Martin and Kauffman* [1977] operates at a higher density ratio and does coincide with the values obtained from our simulations (cf. Figure 4).

6.3. The Melt Rate

The determination of the melt rate from the three-equation formulation requires knowledge of two parameters: the bulk heat exchange coefficient, α_h, and the boundary thickness ratio, R. The latter is relevant for the determination of the interface temperature, T_i. The melt rate is then given as a function of far-field temperature, T_∞, and friction velocity, u_{*0} (see equation (3a)). In this work, we have determined R to be 2.2 ± 0.2. In the absence of temperature and salinity fluxes in the ice, the three-equation formulation yields melt rates that are up to 40% lower than previous estimates due to the influence of R on the interface temperature (see Figure 1b).

Keitzl et al. [2016] have suggested a similarity between freshwater and seawater systems when results are compared in terms of a Richardson number. With the interface temperature available, the melt rates can be provided as a function of the convective Richardson number,

$$\mathrm{Ri}_* = \frac{\Delta b z_0}{w_*^2}, \tag{23}$$

with the strength of the stable stratification, $\Delta b = b(z_i) - b_m$, the thickness of the diffusive interface layer, z_0, and the convective velocity scale, w_* (see Figure 7). The convective Richardson number describes the ratio between the kinetic energy that a fluid particle needs to overcome the diffusive shield beneath the ice and its actual kinetic energy.
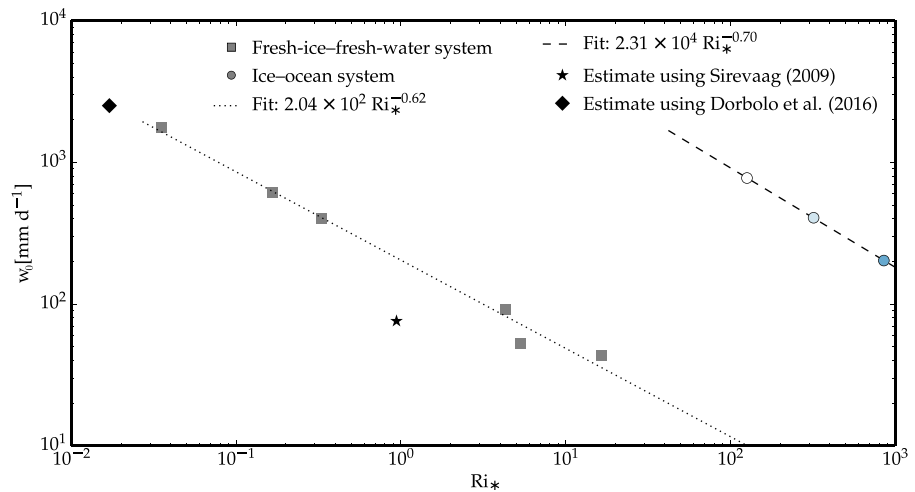
Figure 7. Melt rates, w_0, over convective Richardson number, Ri_*. The convective Richardson numbers of the simulations are determined from the strength and apparent position of the buoyancy-reversal instability and the convective velocity scale (filled circles). Colors indicate the density ratio, R_ρ^s, as given in Figure 3c. The convective Richardson number of the freshwater system is taken from *Keitzl et al.* [2016] (filled squares). The melt rates of the freshwater system agree well with independent laboratory measurements of *Dorbolo et al.* [2016] (black diamond). They measured the mass flux of a rotating ice disc melting in fresh water. From PIV measurements, they found convective velocities of 10 mm s^{-1} at a far-field temperature of 20°C (personal communication). The turbulent-instrument-cluster measurements of *Sirevaag* [2009] follow more closely our simulations of the freshwater system than those of the ice–ocean system (black star). His measurements of far-field conditions and friction velocity allow us to reconstruct a convective Richardson numbers, where we used $R = 2.15$. We assess his measurement in the section 6.

A comparison of the Richardson-number dependence of the melt rates measured from our simulation (see Figure 7, filled circles) to that of the freshwater system (see Figure 7, filled squares), shows how both systems follow a similar working principle. As the far-field temperature increases, the buoyancy-reversal instability strengthens and the convective Richardson number decreases (see Figure 7, filled circles). With increasing convective motion beneath the ice, the melt rates of the ice increase. Compared to the ice–ocean system, the freshwater system has larger an extent of the diffusive interface layer but significantly weaker a diffusive shield at similar free-convection velocities for systems of similar size. Consequently, the Richardson numbers of the freshwater system with similar melt rates are smaller by a factor of 100. In this case, convective motions are strong enough to overcome the diffusive shield. In the case of ice–ocean free convection, however, we have observed that convective motions were not strong enough to overcome the diffusive shield.

The melt rates in conditions of forced convection and mixed convection remain to be ascertained. *Sirevaag* [2009] provides a well-controlled field measurement of mixed convection in ice–melting conditions. He measured the far-field temperature (-0.86 °C), the far-field salinity (34.4 psu), the heat flux (268 W m^{-2}) and the friction velocity (0.9×10^{-2} m s^{-1}). From his measurements, we reproduce the interface temperature (-1.27 °C), the interface salinity (23.5 psu), the buoyancy shielding Δb (8.8×10^{-2} m s^{-2}), and the minimum buoyancy b_m (-1.5×10^{-4} m s^{-2}). If his heat-flux measurement under the given mixed-convection conditions is representative for the diffusive flux at the interface, we estimate $z_0 = 0.9 \times 10^{-3}$ m. In the absence of fluxes within the ice, his measurements yield a melt rate of 76 mm d^{-1} at a convective Richardson number of about 1. His measurement deviates thus from the Richardson-number dependence seen for the simulated ice–ocean system and follows more closely the simulated freshwater system.

From the measurements of *Sirevaag* [2009], we learn that mixed convection occurs at lower Richardson numbers because turbulent motions eventually compete with the diffusive shield just as in freshwater free convection. From the minimum buoyancy, b_m, and the stably stratified buoyancy shield, Δb, one expects a reference Richardson number, equation (13), for his measurement of about 585 and hence a density ratio parameter $R_\rho^s \sim 585$ (see equation (14)). If the measurement were made under free-convection conditions, one further expects a turbulent-flux ratio of about 1350 (from equation (21)). Instead *Sirevaag* [2009] found $\gamma_{turb} = 33$. We conjecture that in mixed convection, the influence of external

forcing tends to even out differences between the turbulent fluxes of heat and salt but does not fully succeed to do so. The role of the density ratio, R_ρ^s, in sustaining the convective motion decreases with the strength of shear. In the limit of forced convection, according to Reynolds analogy [*Tennekes and Lumley*, 1972], one might hence expect a turbulent-flux ratio that is not influenced by R_ρ^s anymore and approaches order of one.

6.4. The Turbulent-Flux Ratio Under Ice–Growing Conditions

Even though we have considered a melting–ice scenario for our studies, we now assess the turbulent-flux ratio of a growing–ice scenario. *McPhee et al.* [2008] study the double-diffusive tendencies under growing ice. They found an asymmetric behavior of the double-diffusive process between freezing and melting ice: While turbulent-flux ratios measured in melting–ice scenarios are of order 10^1 to 10^2, the turbulent-flux ratio in growing–ice scenarios was assessed to be unity. As opposed to melting ice, they suggest that for growing ice the double-diffusive tendencies are relieved by dynamics within the mushy layer above the advancing ice front.

This mushy layer prevails for growing ice because the salt of the ocean water is embedded between growing ice crystals. As long as ice continues to grow, the lower most advancing front of bulk ice will always embed salt corresponding to the salinity of the ocean water as it grows [*Notz and Worster*, 2009]. Therefore, we do not expect any salt gradient between the ocean water and the lower most front of the mushy layer. The interface salinity is that of the ocean water.

The presence of an interface salinity lower than the salinity in the outer layer is a prerequisite for the promotion of the buoyancy-reversal instability. In the absence of the buoyancy-reversal instability (the forcing mechanism of free convection), the density ratio, R_ρ^s, does no longer control nor influence the ratio in which salinity and temperature mix in the outer layer. The convection that remains is for example forced by draining salt plumes or by vertical shear due to the drifting of ice. Forced convection, however, does not distinguish between the mixing of temperature and salinity, because—by definition—the diffusivities do not influence the turbulent-flux ratio (see equation (18)). Based on our findings, we expand the argument of *McPhee et al.* [2008]; not dynamics within the mushy layer but its mere presence implies a turbulent-flux ratio of unity.

7. Summary and Conclusions

The main objective of this study has been the analysis of the ratio of heat and salt fluxes. This flux ratio is used in models of ice–ocean interaction to control the interface conditions and thus also the melt rates. We have obtained the vertical structure of the flux ratio from simulations of free convection beneath a melting, horizontal, smooth ice–ocean interface in the semiconvective regime. By means of direct numerical simulations, we have determined the flux ratio for the first time not only in the outer layer but also directly at the interface. We have reported the following main findings.

First, the ratio of heat and salt fluxes has the following vertical structure: in the outer layer, the ratio depends strongly on the far-field temperature and salinity of water. A commonly used independent control parameter, the density ratio, R_ρ^s, can be used to scale the flux ratio there in the case of free convection studied here. Next to the interface, however, the flux ratio becomes almost independent of the far-field conditions as has been indicated before by *Holland and Jenkins* [1999]. The flux ratio has to be evaluated at the interface to obtain the value relevant for the determination of the ice–ocean interface conditions. Our simulations indicate that direct measurements of the interface flux ratio based on the turbulent fluxes will be difficult, because next to the interface the turbulent contribution ceases and is not a good proxy for the molecular contribution. Instead we have presented a consistent evaluation of the flux ratio based on the total heat and salt fluxes.

Second, our results support that whenever buoyancy forcing contributes to the driving of ocean turbulence, the turbulent-flux ratio in the outer layer should deviate from unity toward $2.3R_\rho^s$.

Third, the interface flux ratio is 3 times as large as previously assessed based on turbulent-flux measurements away from the interface. Instead of the flux ratio currently used, $\gamma_{\mathrm{turb}} = 33$, which corresponds to the turbulent-flux ratio in the outer layer, we find $\gamma_i \approx 83$–100 to be more realistic at the interface. With γ_i the

interface conditions are determined according to equations (1c) and (4). Compared to our new estimate, melt rates of the ice–ocean interface based on the three-equation formulation using the too low value γ_{turb} =33 are overestimated by up to 40%.

References

Carpenter, J. R., T. Sommer, and A. Wüest (2012), Simulations of a double-diffusive interface in the diffusive convection regime, *J. Fluid Mech.*, *1*, 1–26, doi:10.1017/jfm.2012.399.

Dorbolo, S., N. Adami, C. Dubois, H. Caps, N. Vandewalle, and B. Darbois-Texier (2016), Rotation of melting ice disks due to melt fluid flow, *Phys. Rev. E*, *93*, 1–5, doi:10.1103/PhysRevE.93.033112.

Gade, H. G. (1993), When ice melts in sea water: A review, *Atmos. Ocean*, *31*, 139–165, doi:10.1080/07055900.1993.9649466.

Gargett, A. E., W. J. Merryfield, and G. Holloway (2003), Direct numerical simulation of differential scalar diffusion in three-dimensional strat-ified turbulence, *J. Phys. Oceanogr.*, *33*, 1758–1782, doi:10.1175/2403.1.

Holland, D. M., and A. Jenkins (1999), Modeling thermodynamic ice–ocean interactions at the base of an ice shelf, *J. Phys. Oceanogr.*, *29*, 1787–1800, doi:10.1175/1520-0485(1999)029 < 1787:MTIOIA>2.0.CO;2.

Johnston, H., and C. R. Doering (2009), Comparison of turbulent thermal convection between conditions of constant temperature and con-stant flux, *Phys. Rev. Lett.*, *102*(6), 064501, doi:10.1103/PhysRevLett.102.064501.

Josberger, E. G. (1983), Sea ice melting in the marginal ice zone, *J. Geophys. Res.*, *88*, 2841–2844, doi:10.1029/JC088iC05p02841.

Keitzl, T., J. P. Mellado, and D. Notz (2016), Impact of thermally driven turbulence on the bottom melting of ice, *J. Phys. Oceanogr.*, *46*, 1171–1187, doi:10.1175/JPO-D-15-0126.1.

Kimura, S., and W. Smyth (2007), Direct numerical simulation of salt sheets and turbulence in a double-diffusive shear layer, *Geophys. Res. Lett.*, *34*, L21610, doi:10.1029/2007GL031935.

Lele, S. K. (1992), Compact finite difference schemes with spectral-like resolution, *J. Comput. Phys.*, *103*, 16–42, doi:10.1016/0021-9991(92)90324-R.

Martin, S., and P. Kauffman (1977), An experimental and theoretical study of the turbulent and laminar convection generated under a horizontal ice sheet floating on warm salty water, *J. Phys. Oceanogr.*, *7*, 272–283, doi:10.1175/1520-0485(1977)007 < 0272:AEATSO> 2.0.CO;2.

McPhee, M., J. H. Morison, and F. Nilsen (2008), Revisiting heat and salt exchange at the ice–ocean interface: Ocean flux and modeling con-siderations, *J. Geophys. Res.*, *113*, C06014, doi:10.1029/2007JC004383.

McPhee, M. G. (1981), An analytic similarity theory for the planetary boundary layer stabilized by surface buoyancy, *Boundary Layer Mete-orol.*, *21*, 325–339, doi:10.1007/BF00119277.

McPhee, M. G., G. A. Maykut, and J. H. Morison (1987), Dynamics and thermodynamics of the ice/upper ocean system in the marginal ice zone of the Greenland Sea, *J. Geophys. Res.*, *92*, 7017–7031, doi:10.1029/JC092iC07p07017.

Mellado, J., and C. Ansorge (2012), Factorization of the Fourier transform of the pressure-Poisson equation using finite differences in colo-cated grids, *Z. Angew. Math. Mech.*, *92*, 380–392, doi:10.1002/zamm.201100078.

Mellado, J. P. (2012), Direct numerical simulation of free convection over a heated plate, *J. Fluid Mech.*, *712*, 418–450, doi:10.1017/jfm.2012.428.

Mellado, J. P., C. C. Heerwaarden, and J. R. Garcia (2016), Near-surface effects of free atmosphere stratification in free convection, *Boundary Layer Meteorol.*, *159*, 69–95, doi:10.1007/s10546-015-0105-x.

Nagashima, H., J. Yoshida, and Y. Nagahama (1997), A three dimensional modeling of salt-fingering convection, in *Proceedings of an Inter-national Congress on Modeling and Simulation*, vol. 1, pp. 189–191, Modell. and Simul. Soc. of Aust. & N. Z., Perth, Australia.

Notz, D., and M. G. Worster (2009), Desalination processes of sea ice revisited, *J. Geophys. Res.*, *114*, C05006, doi:10.1029/2008JC004885.

Notz, D., M. G. McPhee, M. G. Worster, G. A. Maykut, K. H. Schlünzen, and H. Eicken (2003), Impact of underwater-ice evolution on Arctic summer sea ice, *J. Geophys. Res.*, *108*(C7), 3223, doi:10.1029/2001JC001173.

Owen, P. R., and W. R. Thomson (1963), Heat transfer across rough surfaces, *J. Fluid Mech.*, *15*, 321–334, doi:10.1017/S0022112063000288.

Pope, S. B. (2000), *Turbulent Flows*, Cambridge Univ. Press, Cambridge, U. K.

Rohatgi, A. (2014), *Version 3.3 of WebPlotDigitizer*, Zenodo, Genève, Swiss, doi:10.5281/zenodo.10532.

Schmidt, G. A., C. M. Bitz, U. Mikolajewicz, and L.-B. Tremblay (2004), Ice–ocean boundary conditions for coupled models, *Ocean Modell.*, *7*, 59–74, doi:10.1016/S1463-5003(03)00030-1.

Sharqawy, M. H., J. H. Lienhard, and S. M. Zubair (2010), Thermophysical properties of seawater: A review of existing correlations and data, *Desalination*, *16*, 354–380, doi:10.5004/dwt.2010.1079.

Sirevaag, A. (2009), Turbulent exchange coefficients for the ice/ocean interface in case of rapid melting, *Geophys. Res. Lett.*, *36*, L04606, doi: 10.1029/2008GL036587.

Sommer, T., J. R. Carpenter, M. Schmid, R. G. Lueck, M. Schurter, and A. Wüest (2013), Interface structure and flux laws in a natural double-diffusive layering, *J. Geophys. Res. Oceans*, *118*, 6092–6106, doi:10.1002/2013JC009166.

Steele, M., G. L. Mellor, and M. G. Mcphee (1989), Role of the molecular sublayer in the melting or freezing of sea ice, *J. Phys. Oceanogr.*, *19*, 139–147, doi:10.1175/1520-0485(1989)019 < 0139:ROTMSI>2.0.CO;2.

Tennekes, H., and J. L. Lumley (1972), *A First Course in Turbulence*, MIT Press, Cambridge, Mass.

Turner, J. S. (1974), Double-diffusive phenomena, *Annu. Rev. Fluid Mech.*, *6*, 37–54, doi:10.1146/annurev.fl.06.010174.000345.

Williamson, J. H. (1980), Low-storage Runge-Kutta schemes, *J. Comput. Phys.*, *35*, 48–56, doi:10.1016/0021-9991(80)90033-9.

Wilson, N., T. Sarma, and R. Pritchard (1980), Prediction of heat, mass, and momentum transfer during laminar forced convective melting of ice in saline water, sea ice processes and models, in *Proceedings of the Arctic Ice Dynamics Joint Experiment International Commission of Snow and Ice Symposium*, 339 pp., Univ. of Wash. Press, Seattle.

Yaglom, A. M., and B. A. Kader (1974), Heat and mass transfer between a rough wall and turbulent fluid flow at high Reynolds and Péclet numbers, *J. Fluid Mech.*, *62*, 601–623, doi:10.1017/S0022112074000838.

Zweigle, T. (2011), Direkte numerische Simulation von Salzfingern—Direct numerical simulation of saltfingers, PhD thesis, Univ. of Bremen, Bremen, Germany.